ACS NANO

www.acsnano.org

ARTICLE

Enhancement of Photoresponse on Narrow-Bandgap Mott Insulator α-$RuCl_3$ *via* Intercalation

Min-kyung Jo, Hoseok Heo, Jung-Hoon Lee, Seungwook Choi, Ansoon Kim, Han Beom Jeong, Hu Young Jeong, Jong Min Yuk, Daejin Eom, Junghoon Jahng, Eun Seong Lee, In-young Jung, Seong Rae Cho, Jeongtae Kim, Seorin Cho, Kibum Kang,* and Seungwoo Song*

Cite This: *ACS Nano* 2021, 15, 18113–18124

Read Online

ACCESS | Metrics & More | Article Recommendations | Supporting Information

ABSTRACT: **Charge doping to Mott insulators is critical to realize high-temperature superconductivity, quantum spin liquid state, and Majorana fermion, which would contribute to quantum computation. Mott insulators also have a great potential for optoelectronic applications; however, they showed insufficient photoresponse in previous reports. To enhance the photoresponse of Mott insulators, charge doping is a promising strategy since it leads to effective modification of electronic structure near the Fermi level. Intercalation, which is the ion insertion into the van der Waals gap of layered materials, is an effective charge-doping method without defect generation. Herein, we showed significant enhancement of optoelectronic properties of a layered Mott insulator, α-$RuCl_3$, through electron doping by organic cation intercalation. The electron-doping results in substantial electronic structure change, leading to the bandgap shrinkage from 1.2 eV to 0.7 eV. Due to localized excessive electrons in $RuCl_3$, distinct density of states is generated in the valence band, leading to the optical absorption change rather than metallic transition even in substantial doping concentration. The stable near-infrared photodetector using electronic modulated $RuCl_3$ showed 50 times higher photoresponsivity and 3 times faster response time compared to those of pristine $RuCl_3$, which contributes to overcoming the disadvantage of a Mott insulator as a promising optoelectronic device and expanding the material libraries.**

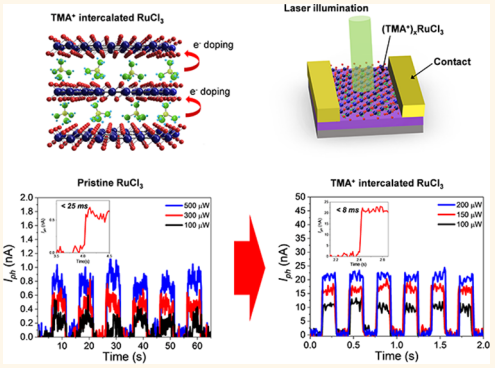

KEYWORDS: *two-dimensional materials, Mott insulator, intercalation, charge doping, optoelectronic properties*

INTRODUCTION

Intercalation is an effective approach to modify the properties of two-dimensional (2D) layered materials by incorporating guests into their interlayer spacing. Various properties such as the optical,[1,2] magnetic,[3−5] thermoelectric,[6] electrical transport,[7−9] and telecommunication[10] of 2D materials have been modified or improved *via* intercalation.

Among the applications including transistors,[11,12] memory devices,[13,14] and catalysts,[15,16] 2D layered materials have garnered attention as the most potential semiconducting materials for optoelectronic devices attributed to their sizable bandgap.[17] However, application for near-infrared (NIR) detection is limited compared to that of the visible range because of the narrow candidates of stable 2D materials having a bandgap around 0.5−0.8 eV.[18] Unlike other properties, tuning of the bandgap *via* ion intercalation is intrinsically limited because it leads to metallic transition due to concomitant charge doping during the process. For example, semiconducting 2H-MoS_2 goes through a phase transition into metallic 1T-MoS_2 by Li^+ ion intercalation as degenerated silicon with a high level of doping.[19]

On the other hand, it is possible to change the optical bandgap rather than semiconductor-to-metallic transition *via* intercalation if the doped electrons are localized instead of freely moving. Mott insulators, which have especially strong electron−electron repulsion not as in conventional semiconductors,[20] are candidates for the phenomenon. The large Coulomb repulsion energy U between two electrons overcomes the kinetic energy t, resulting in its insulator

Received: August 6, 2021
Accepted: November 1, 2021
Published: November 4, 2021

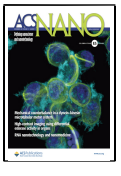

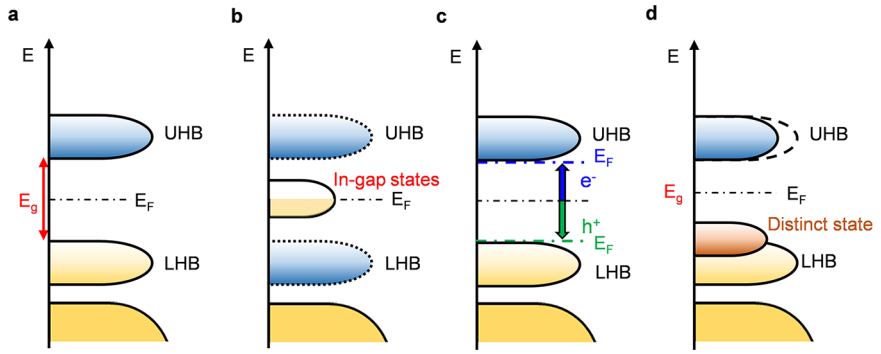

Figure 1. Band structures of the pristine and charge-doped Mott insulators. (a) Mott insulators, d states split into a lower- and upper-Hubbard band (LHB and UHB) with the Mott gap. When doping with electrons, conventional scenarios are (b) formation of the in-gap states at the Fermi level or (c) the modification of the Fermi level toward the edge of UHB. (d) Special change in the electronic states for electron doping in α-$RuCl_3$.

behaviors;[21] otherwise, they would be metals according to conventional band theory.

α-$RuCl_3$ is a layered material having spin−orbit coupling (SOC)-assisted Mott insulating nature with a 2D honeycomb lattice.[22] Interestingly, a substantial degree of electron doping *via* surface adsorption or intercalation of alkali metal ions in α-$RuCl_3$ leads to bandgap shrinkage with NIR absorption instead of metallic transition in previous reports.[23−25] Considering that most Mott insulators are studied to go through insulator-to-metallic transition or even superconducting transition under charge doping,[26] the retention of the bandgap in $RuCl_3$ after electron doping is characteristic. Due to the localization of excess electrons in $RuCl_3$,[24] it showed unusual bandgap change.

The optical bandgap change in $RuCl_3$ is also different from Burstein−Moss shift, which is the optical bandgap increase resulting from the high degree of electron doping in conventional semiconductors. When the conventional semiconductors are degenerated due to excessive electron doping, the absorption edge is shifted toward the states within the conduction band, resulting from the Fermi level shift. In contrast, the electron doping of $RuCl_3$ does not accompany the Fermi level change and leads to the bandgap reduction from band structure change.

As a result, electron localization hosted in the 2D layered Mott insulator $RuCl_3$ renders it to be a perfect system for tuning the optical bandgap *via* ion intercalation. However, it is difficult to demonstrate a device using alkali metal ion intercalated α-$RuCl_3$ because of the instability of an alkali metal ion in ambient atmospheric conditions.[27] For the synthesis of stable electron-doped α-$RuCl_3$, we introduced the intercalation of organic molecules into layered α-$RuCl_3$. With the thermodynamically favorable combination of α-$RuCl_3$ with an intercalant (sometimes called guest molecule), the tetramethylammonium ion (TMA^+), the intercalation occurs under mild heating in the ambient air. The $(TMA^+)_xRuCl_3$ superlattice had a stable structure for more than four months and showed an optical absorption of NIR centered at 0.7 eV, which was 500 meV lower than pristine absorption. The dramatic reduction of the optical bandgap originates from the distinct density of states (DOS) generated in the valence band nearer to the Fermi level.

In this study, we successfully demonstrated the air-stable and NIR photodetector of 1600 nm absorption, which was forbidden in pristine α-$RuCl_3$ utilizing the $(TMA^+)_xRuCl_3$ superlattice as a channel material. Pristine α-$RuCl_3$ as a channel material did not respond to the 1600 nm light source because the optical absorption took place above 1 eV. In contrast, the photodetector with the $(TMA^+)_xRuCl_3$ superlattice was stably operated under a 1600 nm light source. In comparison with the pristine photodetector under 1100 nm illumination, the intercalated photodetector under 1600 nm light exhibited 50 times higher responsivity and three times faster response time. Considering that optoelectronic devices utilizing Mott insulators have been unsatisfactory due to low photocurrent,[28,29] the organic ion intercalation not only changes the optical bandgap in a desirable way but also enhances the optoelectronic properties.

RESULTS AND DISCUSSION

In general, Mott insulators have an energy gap called the Mott−Hubbard (M−H) gap in the transition-metal d states originating from the large Coulomb repulsion energy U between two electrons. It leads to the splitting of d states into a upper- and a lower-Hubbard band (UHB and LHB) with an M−H gap across the Fermi level.[21] The exact electronic structure of α-$RuCl_3$ could be described considering SOC as well as electron−electron repulsion (Figure S1, Supporting Information). Under octahedral symmetry, 4d states are split into higher energy e_g and lower energy t_{2g} states. In general, $4d^5$ transition-metal oxide or halide shows a t^5_{2g} low-spin configuration due to a sufficiently large crystal field. When the moderate spin−orbit interaction is taken into account, the t_{2g} band is split into an effective total angular momentum $J_{eff} = 1/2$ doublet and $J_{eff} = 3/2$ quartet bands.[30−32] Despite the smaller value of the spin−orbit interaction compared to that of $5d^5$ Mott insulators,[33,34] many of the theoretical calculations or experimental results reported that spin−orbit interaction in α-$RuCl_3$ is essential to explain its electronic property.[35−39] Moreover, the less on-site electron−electron repulsion U compared to the Mott insulator with 3d electron configuration is sufficient to open a Mott gap in the $J_{eff} = 1/2$ states, leading to the splitting of UHB and LHB across the Fermi level.[21] Since $J_{eff} = 3/2$ quartet band and LHB of $J_{eff} = 1/2$ are fully occupied by five 4d electrons, α-$RuCl_3$ has an insulating nature, as shown in Figure 1a. Typically, insulating phases of Mott insulators are easily collapsed by charge doping, which is called the metal-to-insulator transition (MIT). The charge carrier doping into Mott insulators is one of the key strategies for obtaining superconductors with high transition temperature.[26,40,41]

https://doi.org/10.1021/acsnano.1c06752
ACS Nano 2021, 15, 18113−18124

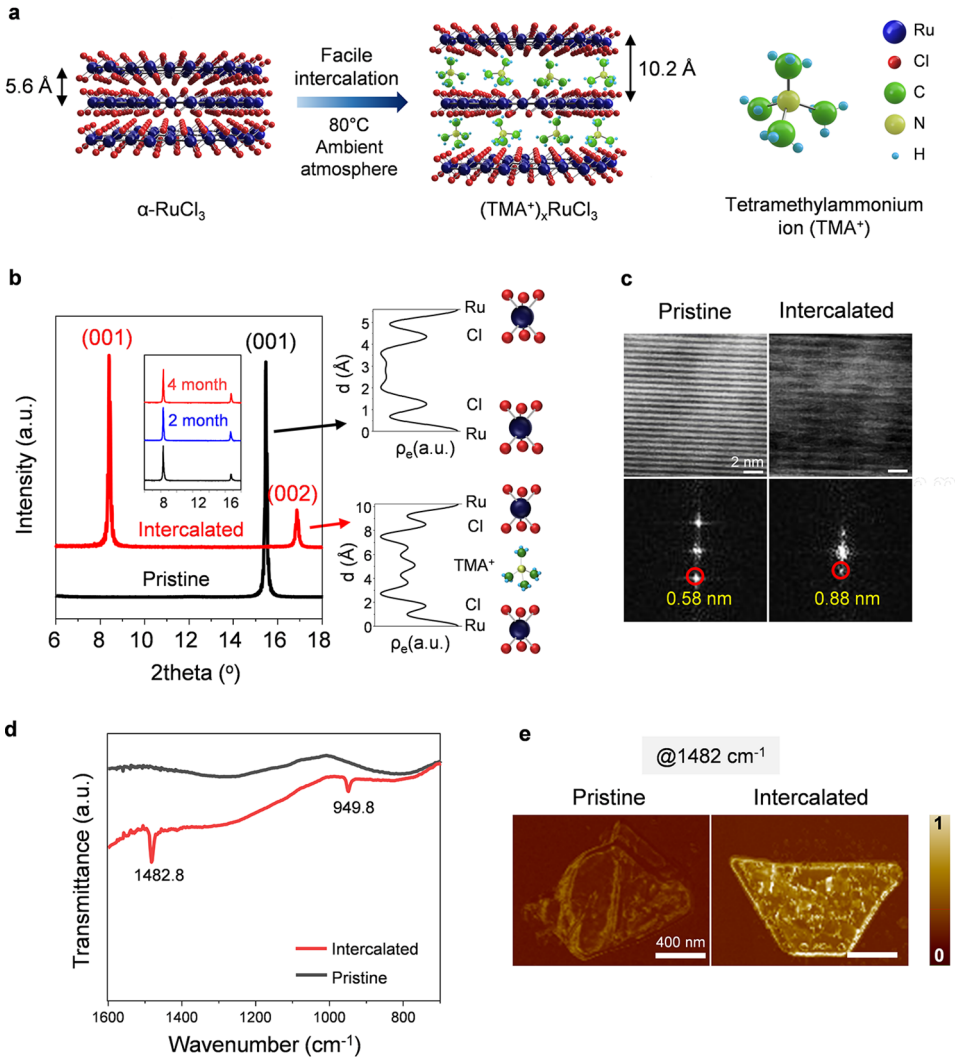

Figure 2. Schematics and characterizations of the facile α-$RuCl_3$ intercalation. (a) Schematics of the chemical intercalation of α-$RuCl_3$. (b) Selected X-ray diffraction (XRD) spectra of the pristine α-$RuCl_3$ and $(TMA^+)_xRuCl_3$ (left). The intercalated superlattice kept its structure for more than four months (inset). The corresponding one-dimensional electron density along the *c*-axis (right). (c) Cross-sectional high-resolution transmission electron microscopy (HRTEM) image comparison between the pristine $RuCl_3$ and $(TMA^+)_xRuCl_3$ and the corresponding fast Fourier transformation images with a scale bar of 2 nm. (d) Fourier transformation infrared spectroscopy (FT-IR) spectra of pristine $RuCl_3$ and $(TMA^+)_xRuCl_3$. (e) Photoinduced force microscopy (PiFM) image of pristine $RuCl_3$ and $(TMA^+)_xRuCl_3$ at 1482 cm^{-1}. $(TMA^+)_xRuCl_3$ has a higher PiFM signal due to the intercalation of the TMA^+ ion with a scale bar of 400 nm.

Conventionally, the consequences of doping for Mott insulators can be explained by two scenarios. The first one is the formation of "in-gap states", as represented in Figure 1b. Cai *et al.* tracked the electronic structure with increasing hole-doping concentration of $Bi_2Sr_{2-x}La_xCuO_{6+\delta}$ from insulating phase to the superconducting regime.[42] They discovered that in-gap states emerged within the original gap of the parent cuprates with a small doping concentration. As doping concentration increased, the in-gap spectral weight was increased and the gap between in-gap states became narrower to 12 MeV. The second scenario is the shift of chemical potential toward the conduction (valence) band upon electron (hole) doping, as shown in Figure 1c. Battisti *et al.* visualized the evolution of the electronic states of electron-doped $(Sr_{1-x}La_x)_2IrO_4$.[43] In this case, the electron doping did not change the Mott gap size until a certain threshold doping concentration. When the threshold concentration was reached, the Fermi level was abruptly pinned closer to the bottom of the UHB, leading to a metallic nature.

However, upon electron doping of α-$RuCl_3$ *via* intercalation, the MIT transition was not observed, even with a substantial degree of doping. There was an abrupt spectral weight transfer in the valence band near the Fermi level as soon as the electron was doped into the system, as presented in Figure 1d. The position of the distinct DOS generated in the valence band does not vary with the doping concentration. The portion of the generated one increases while that of the original UHB is suppressed. This phenomenon is interesting in that it does not accompany a metallic transition. Instead, the optical absorption peak shifts to lower energy and the peak position keeps along with the doping concentration. Considering that cuprates require ~5% of doping for superconducting transition,[44] the insulating property of α-$RuCl_3$ persists until an extraordinary doping concentration.

https://doi.org/10.1021/acsnano.1c06752
ACS Nano 2021, 15, 18113−18124

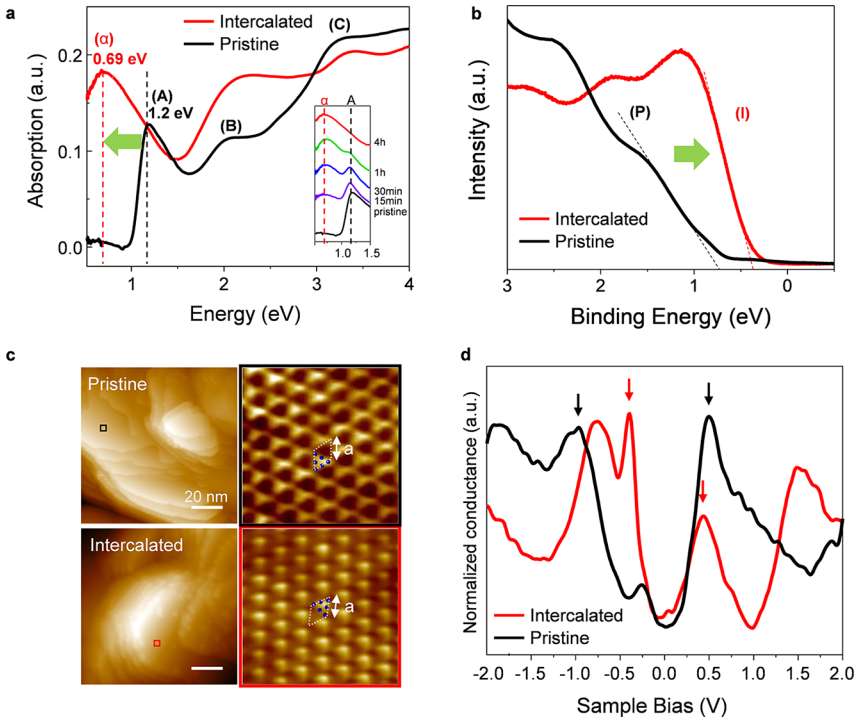

Figure 3. Optical property tuning *via* intercalation and the underlying band structure modification. (a) UV−vis absorption spectrum of pristine and intercalated α-$RuCl_3$. (b) Valence-band photoemission spectrum of pristine and intercalated $RuCl_3$. (c) Scanning tunneling microscopy (STM) constant current images of pristine (top) and intercalated (bottom) $RuCl_3$. Each right figure is the blown-up image of the rectangular region in the corresponding left figure. They are probed with a sample bias of 0.3 V. The lozenge in the right figure represents the in-plane unit cell with the lattice parameter, *a*, of 5.98 Å and the blue solid dots indicate Ru ions in unit cell. (d) Scanning tunneling spectroscopy (STS) spectra of pristine (black) and intercalated (red) $RuCl_3$.

In this study, to explore the modification of optical properties by intercalation, we used a few-layered single-crystalline α-$RuCl_3$ grown by a flux method. Synthesized α-$RuCl_3$ exhibited a typical antiferromagnetic ordering transition at T_N = 14 K, as in other studies,[36,45] where T_N is the Néel temperature (Figure S2). Then, the α-$RuCl_3$ crystal was mechanically exfoliated on quartz or 300 nm SiO_2/Si substrates. α-$RuCl_3$ was intercalated with a TMA^+ ion with a facile chemical intercalation method, as shown in Figure 2a. The substrate containing exfoliated α-$RuCl_3$ was immersed in the TMA^+Br^-/propylene carbonate solution at 80 °C in ambient air for a few hours (Figure S3). The spontaneous intercalation of the TMA^+ ion into α-$RuCl_3$ did not require complicated experimental setups, as in electrochemical intercalation. Moreover, unlike air-unstable alkali metal ion intercalation, intercalation was conducted in ambient atmospheric conditions. This facile intercalation of the alkylammonium ion into α-$RuCl_3$ can be explained with the following equations: $\alpha\text{-}RuCl_3 + x(TMA^+) + Br^- \rightarrow (TMA^+)_xRuCl_3^- + {}^1/_2Br_2$.

Here, we suggest that the driving force of spontaneous intercalation of TMA^+ ion into the α-$RuCl_3$ crystal is electron donation from Br^- of TMA^+Br^- to the surface of α-$RuCl_3$, similar to the n-type doping of WSe_2 reported in previous reports that the Br^- ion in cetyltrimethylammonium bromide (CTA^+Br^-) enabled electron injection.[46] The molecular-donated electron can be localized at transition-metal Ru^{3+} surroundings and reduce transition-metal ions due to the Mott insulating nature of α-$RuCl_3$. The reduction of Ru^{3+} is exceptionally favorable because Ru^{2+} centers have low spin, diamagnetic d^6 character. The d^6 electron configuration has special stability, which originates from the ligand field stabilization energy.[47] Therefore, the spontaneous intercalation of a TMA^+ ion into $RuCl_3$ is possible under mild conditions. The intercalation of the TMA^+ ion was easier compared to other alkylamines because of its short carbon chain length. The tetraalkylammonium ion, whose alkyl group has more than an ethyl chain, could not be used as a precursor for facile intercalation of α-$RuCl_3$ due to kinetic reasons (not shown here).

The XRD measurement showed that the interlayer distance of $RuCl_3$ was expanded from 5.6 to10.2 Å after intercalation (Figure 2b). The one-dimensional (1D) electron density map, which was calculated from the XRD (00l) peaks, successfully described the electron density of the TMA^+ ion between the α-$RuCl_3$ slabs after intercalation. The intercalated superlattice kept its structure even after four months in ambient air conditions, indicating the superior stability of the superlattice. Moreover, the $(TMA^+)_xRuCl_3$ superlattice sustains its structure when it is immersed in any polar solvents that are usually used in device fabrication processes. Atomic force microscopy (AFM) analysis confirmed the increment of the height of the α-$RuCl_3$ flake after intercalation, which corresponded well to the interlayer space change measured by XRD (Figure S4). The increment of interlayer distance was further confirmed by a cross-sectional image of pristine α-$RuCl_3$ and the $(TMA^+)_xRuCl_3$ superlattice by HRTEM shown in Figure 2c. Fast Fourier transformation of both specimens revealed that the interlayer distance of α-$RuCl_3$ increased from 5.8 Å to 8.8 Å by intercalation. Although the interlayer distance after intercalation was not matched perfectly with the XRD and AFM results due to the superlattice's fragility to Ga and the

https://doi.org/10.1021/acsnano.1c06752
ACS Nano 2021, 15, 18113−18124

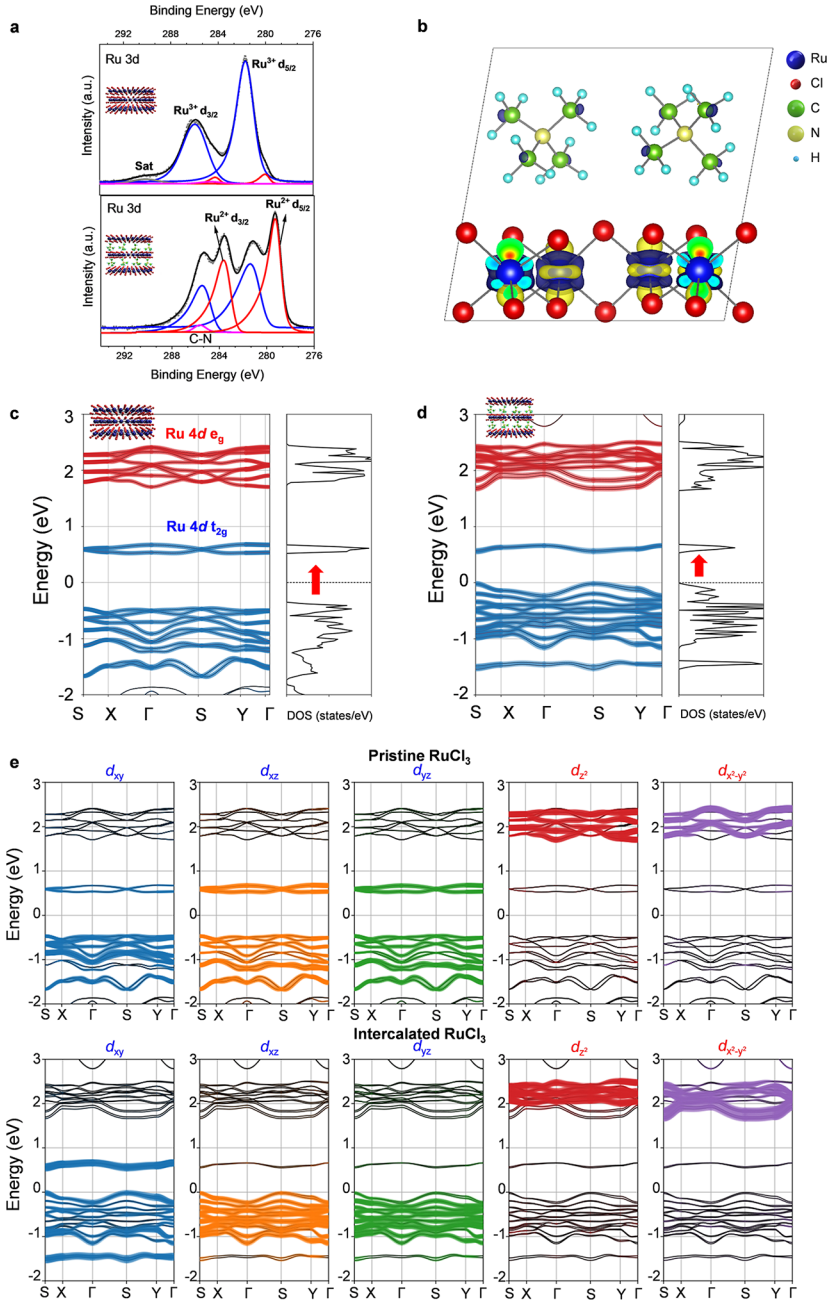

Figure 4. Localized electron doping and electronic band structure modification induced by TMA^+ ion intercalation. (a) Ru 3d core level of the pristine (upper) and intercalated (lower) $RuCl_3$ measured by XPS. Ru was reduced from Ru^{3+} (blue) to Ru^{2+} (red) due to electron doping by TMA^+ ion intercalation. (b) Isosurface plots of the charge density difference for intercalated $RuCl_3$. Yellow and blue isosurfaces represent the excessive and deficient charge densities, respectively. The isosurface level is equal to 0.006 e/Bohr^3. (c) Band structure and total DOS of pristine α-$RuCl_3$ and (d) $(TMA^+)_xRuCl_3$ superlattice. (e) Computed orbital-resolved band structures of pristine α-$RuCl_3$ (upper) and $(TMA^+)_xRuCl_3$ superlattice (lower). Five Ru 4d orbitals are indicated by different colors.

electron beam, all the above analyses well reflect the increment of the interlayer spacing of the $RuCl_3$ by TMA^+ ion intercalation.

On the other hand, the existence of an intercalated TMA^+ ion was directly proved by Fourier transform infrared (FT-IR) spectroscopy and photoinduced force microscopy (PiFM) (Figure 2c and d).[48] Before intercalation, pristine α-$RuCl_3$ did not exhibit a discrete absorption peak in the 700−2000 cm^{-1} range. However, the intercalated superlattice had characteristic absorption peaks centered at 950 and 1483 cm^{-1}. The absorption peaks at 950 and 1483 cm^{-1} corresponded to C−H bonds, as in the FT-IR spectrum of the TMA^+Br^- salt (Figure S5). The incorporation of a TMA^+ ion into the superlattice could be spatially resolved by PiFM analysis when the IR light of 1482 cm^{-1} wavenumber was irradiated onto the sample, as shown in Figure 2d and Figure S6. If the sample absorbed light due to the molecular vibration, the thermal expansion of the sample manifests and would be enhanced by the tip-enhanced field, leading to a higher PiFM amplitude called nano-IR absorption. Compared to the pristine α-$RuCl_3$, the intercalation superlattice had a higher nano-IR absorption signal over the entire crystal region, which indicated the

https://doi.org/10.1021/acsnano.1c06752
ACS Nano 2021, 15, 18113−18124

homogeneous intercalation of a TMA^+ ion into the α-$RuCl_3$. The intercalated species was confirmed as a TMA^+ ion rather than tetramethylamine by the N 1s spectra in the X-ray photoelectron spectroscopy (XPS) result (Table S1).[49]

Having confirmed the homogeneous intercalation of a TMA^+ ion into $RuCl_3$, we now address the intercalation effects on the optical properties of the $(TMA^+)_xRuCl_3$ superlattice. Using ultraviolet−visible (UV−vis) spectroscopy, we found that the intercalation of the TMA^+ ion drastically altered the optical absorption of α-$RuCl_3$ as represented in Figure 3a. Our measured UV−vis absorption spectrum of the pristine α-$RuCl_3$ well agreed with previous reports.[37,50,51] For the electronic structure of α-$RuCl_3$, the valence-band maximum band consisted of Ru 4d electrons.[24] As shown in Figure 3a, the strong absorption peak at 1.2 eV (A) was assigned as interband transitions across the M−H gap, namely, $d^5d^5 \rightarrow d^4d^6$ (LHB → UHB). Excitation B centered at E = 2.1 eV could be associated with cubic crystal field splitting, which is excitations into the e_g states. Peak C originated from Cl 3p−Ru 4d charge transfer excitations. The broad features of both peaks reflect the pronounced dispersion of Cl 3p bands.[21] After intercalation, the strong absorption peak A completely vanished, while an absorption peak α centered at 0.69 eV was developed. When the degree of intercalation was reasonably controlled by varying the immersion time, the absorption peak of pristine α-$RuCl_3$ was gradually decreased, while the generated absorption peak by intercalation increased instead (Figure 3a inset and Figure S7). It is worthy to note that the position of the peak α is invariant with the degree of intercalation and the Mott gap did not collapse during the whole intercalation process.

To study the reduction of the optical bandgap after intercalation, the DOS in the valence bands of pristine α-$RuCl_3$ and the $(TMA^+)_xRuCl_3$ superlattice were analyzed by ultraviolet photoelectron spectroscopy (UPS). As presented in Figure 3b, the UPS spectrum of the pristine α-$RuCl_3$ shows the strong peak (P) centered at ∼1.55 eV and the onset of the valence band at ∼0.75 eV. The strong peak corresponds to Ru t_{2g} antibonding LHB, in agreement with previous reports.[21,38] After intercalation, the peak centered at ∼1.15 eV (I) appears and the onset of the valence band shifted to the Fermi level with ∼0.25 eV, which is indicated by the green arrow, suggesting the generation of a distinct DOS within the bandgap after intercalation. Because UPS analysis only provided information about the valence band, we conducted STM and spectroscopy (STS) measurements to understand the effect of intercalation on the conduction band as well.

The representative STM images of both pristine α-$RuCl_3$ and the $(TMA^+)_xRuCl_3$ superlattice shown in Figure 3c revealed a well-ordered layered structure (left figures) and a hexagonal lattice with the same in-plane lattice constant value of 5.98 Å (right figures). In the corresponding STS spectra measured on the two sample surfaces (right figures in Figure 3c); however, a dramatic change of local density of states (LDOS) in the valence band was observed (Figure 3d). The peak at ∼−1.0 eV was assigned as the valence-band maximum (VBM) of the pristine α-$RuCl_3$, while the intercalated superlattice had the VBM at ∼−0.4 eV. On the other hand, the position of the conduction band minimum (CBM) had negligible change after the intercalation (∼0.5 eV), although the LDOS of CBM was decreased after the intercalation. The origin of the DOS in the valence band was presumably related to the decreased DOS in the conduction band. As a result, the Mott excitation of $d^5d^5 \rightarrow d^4d^6$ (LHB → UHB, 1.2 eV) was suppressed and the charge fluctuation by doping, $d^6d^5 \rightarrow d^5d^6$ dominantly led to the reduction of optical bandgap (0.69 eV) after intercalation.[24]

To understand the origin of the electronic structure change behind the optical property change, we conducted XPS and density functional theory (DFT) calculations for pristine and intercalated $RuCl_3$. The electron donation from the Br^- ion to pristine $RuCl_3$ reduced the electronic state of $RuCl_3$ from $Ru^{3+}(4d^5)$ to $Ru^{2+}(4d^6)$, which was supported by XPS spectra of the Ru 3d states. Before intercalation, the Ru 3d spectra showed mostly the Ru^{3+} state with negligible Ru^{2+} state (Figure 4a). After intercalation, the intensity of Ru^{3+} $d_{5/2}$ and $d_{3/2}$ peaks largely decreased, while that of Ru^{2+} increased instead. On the other hand, the intensity of the C 1s peak (C−N) apparently increased after intercalation because the guest molecule contained carbon atoms. The appearance of the N 1s peak and no binding energy shift of the Cl 2p level after the intercalation process confirmed the successful TMA^+ intercalation and localized electron doping at the transition metal site (Figure S8). When one molecule of TMA^+ was inserted into $RuCl_3$ slabs, one electron transferred from Br^- to $RuCl_3$. As a result, the effective doping concentration could be calculated from a comparison of the atomic ratio between Ru and N, obtained from XPS analyses. While pristine α-$RuCl_3$ contained no N atom, as in Table S1, the intercalated superlattice had 40% of N compared to the Ru atom. The change in the relative atomic ratio between Ru and Cl was negligible (∼3.0) after intercalation. Therefore, the effective electron doping *via* TMA^+ ion intercalation could be inferred as 1.6 e^- per each $RuCl_3$ unit cell.

The electron doping of α-$RuCl_3$ was further confirmed by the change of magnetic property after intercalation. Before intercalation, α-$RuCl_3$ featured an antiferromagnetic order under $T_N \approx 14$ K. However, the intercalated $RuCl_3$ showed paramagnetic behavior with depressed magnetic moment (Figure S9). Because the $4d^5$ electron configuration of Ru^{3+} is reduced to a $4d^6$ state with a magnetic nonactive state for roughly 40% of the Ru^{2+} centers, the long-range magnetic order is disturbed by charge doping in the Ru ion. Therefore, the intercalated superlattice showed a paramagnetic property, where magnetic susceptibility decayed with increasing temperature with no magnetic transition. A similar magnetic change has been reported in Li intercalated in α-$RuCl_3$.[52]

We performed vdW-corrected DFT calculations to understand the origin of the electronic and optical property changes upon intercalation in $RuCl_3$. To mimic TMA^+ intercalation between $RuCl_3$ layers, we added one excessive electron on each TMA^+ ion and introduced two TMA^0 ions in the unit cell to represent 50% doping concentration. We first analyzed the charge density difference for intercalated $RuCl_3$ to observe the transfer of an additional electron from the TMA^0 ion to $RuCl_3$ as shown in Figure 4b. To do this, we aligned the Cartesian axes to Ru−Cl bonds in the $RuCl_6$ octahedron. We can clearly see additional electron transfer from the TMA^0 ion to the t_{2g} state of the Ru 4d orbital showing reduction of the Ru ion as we expected. In addition, we found that the bandgap decreases due to generation of distinct states introduced by intercalation of the TMA^0 ion near the Fermi level, as shown in Figure 4c and d. In the right panels of Figure 4c and d, one can notice that the DOS of the CBM level decreases while the distinct states are generated in the VBM levels, and this result is in good agreement with our STS measurement. In particular, as

https://doi.org/10.1021/acsnano.1c06752
ACS Nano 2021, 15, 18113−18124

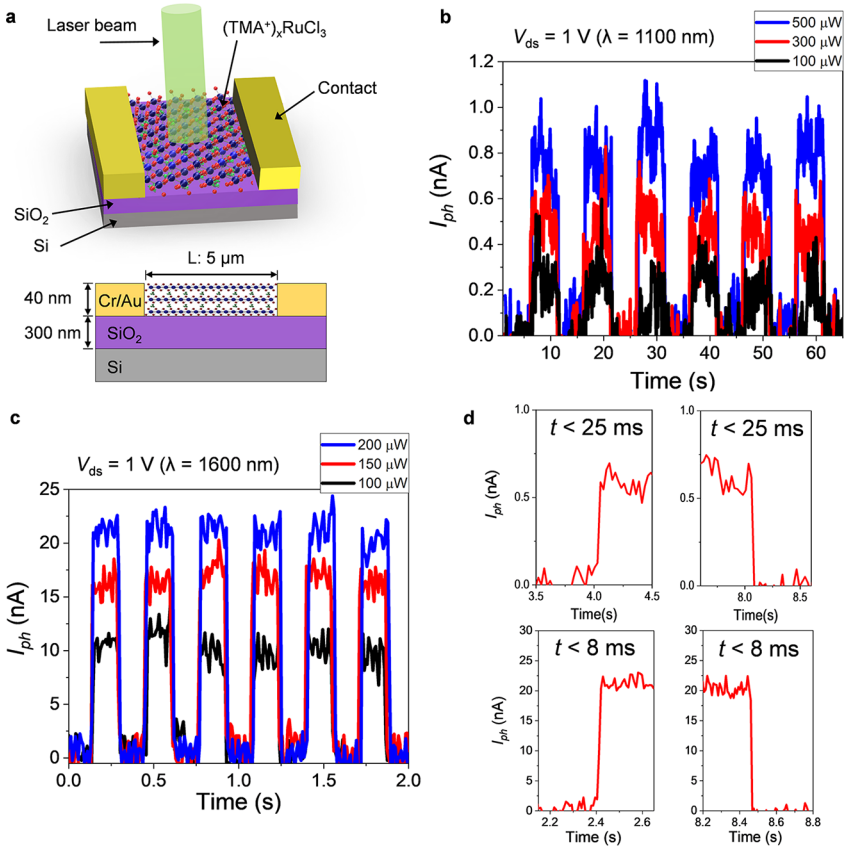

Figure 5. Photoresponse under visible and NIR range illumination for the pristine $RuCl_3$ and $(TMA^+)_xRuCl_3$ photodetector. (a) Schematic diagram of the pristine and intercalated $RuCl_3$ photodetector under laser illumination. (b) Photoswitching characteristics of the pristine α-$RuCl_3$ under modulation of the incident light power (λ = 1100 nm, 180 K) and (c) $(TMA^+)_xRuCl_3$ photodetector under modulation of the incident light power (λ = 1600 nm, 180 K). (d) Temporal current response of the pristine α-$RuCl_3$ and the intercalated $(TMA^+)_xRuCl_3$ photodetector with a rise and decay time of <25 ms and <8 ms, respectively.

shown in Figure 4e, the number of unoccupied Ru $4d_{xz}$ and $4d_{yz}$ states in the CBM level are significantly reduced by intercalation. This suggests that the unoccupied Ru $4d_{xz}$ and $4d_{yz}$ states in the CBM level become occupied by intercalation. Due to this stabilization of the unoccupied Ru 4d t_{2g} states caused by the electron transfer, the computed bandgap (0.541 eV) becomes smaller than that of pristine $RuCl_3$ (0.871 eV), which is in good agreement with our experiment.

To analyze the effect of localized charge doping in the Mott insulator $RuCl_3$, the photoresponse using pristine $RuCl_3$ and the $(TMA^+)_xRuCl_3$ superlattice as channel materials was evaluated under 1100 nm (1.12 eV) and 1600 nm (0.77 eV) laser illumination, respectively, at 180 K. The intercalated two-terminal device was prepared by immersing the pristine device in the TMA^+Br^-/PC solution. The intercalation time was carefully controlled so as not to deteriorate the contact with the Cr/Au metal electrodes. Both pristine and intercalated devices showed linear and symmetric $I_{ds}-V_{ds}$ curves, indicating an ohmic-like contact (Figure S10). After intercalation, the resistance decreased slightly, but the insulating behavior was kept, which was inferred from the temperature-resistance measurement (Figure S11). The intercalation of $RuCl_3$ was easily detected by the color change of a $RuCl_3$ flake through an optical microscope (Figure S12).

Since pristine $RuCl_3$ had an optical absorption above 1 eV, the photoresponse of the photodetector was measured at 1100 nm illumination (1.12 eV). The photocurrent increased upon turning on the incident laser and decayed upon turning off the light (Figure 5b). The typical rise and decay times for the response were characterized as <25 ms (Figure 5d, upper panels). With higher incident laser powers, the photocurrent increased without exceeding 1 nA. The responsivity (R) was acquired from the photocurrent (I_{ph}) at 100 μW illumination and calculated as 4.2×10^{-6} A/W. Responsivity was calculated by the equation $R = I_{ph}/P$ where P is the power of the incident light. On the other hand, under 1600 nm illumination (0.77 eV), the photodetector made of pristine $RuCl_3$ showed no difference between the dark and illuminated states (I_{ph}) (Figure S13).

In contrast, after intercalation, the device represented a photoresponse at 1600 nm attributed to the change in optical absorption. Figure 5c displayed the time-dependent photoresponse of the device under various laser powers. With increasing power, the photocurrent was increased monotonically to ~20 nA. The responsivity (R) of the device was calculated to be 1.0×10^{-4} A/W, which showed 50 times higher responsivity than that of the pristine one with the same irradiation power density. The response time was 3 times faster than that of the pristine one, which showed a rise and decay time of <8 ms. By fitting the I_{ph} and laser power with a simple power law, $I_{ph} \sim P^{\alpha}$, the fitting parameter α was deduced to be ~0.99 (Figure S14). Because α was close to 1, the origin of the photocurrent in the intercalated superlattice was inferred to be not from defect states.[53] It should be noted that the mild doping method *via* intercalation introduced negligible defects into $RuCl_3$.

https://doi.org/10.1021/acsnano.1c06752
ACS Nano 2021, 15, 18113−18124

Many Mott insulators, including undoped cuprates such as $YBa_2Cu_3O_6$, La_2CuO_4, and Nd_2CuO_4, showed ultrafast relaxation and recombination compared to usual semiconductors with similar bandgaps,[54] which was investigated with femtosecond pump−probe spectroscopy.[29,55,56] It can be explained by a strongly bound state called a holon−doublon cluster (HDC, like an exciton) caused by spin−spin interaction as well as the direct Coulomb interaction.[57] Since the formation of HDCs suppressed the photogenerated carrier diffusion along the source−drain bias, it is difficult to extract the carrier from the HDC. Therefore, the external quantum efficiency of the pristine $RuCl_3$ photodetector was sacrificed.

In contrast to the typical Mott insulator, which can derive MIT from carrier doping, the $(TMA^+)_xRuCl_3$ superlattice still sustains its insulating phase after enough electron doping through intercalation. Therefore, we should understand the large improvement of the photoresponse after interaction in α-$RuCl_3$ under the Mott insulator regime. For the electron-doped $(TMA^+)_xRuCl_3$ superlattice, we believe the improvement of the photoresponse compared to pristine $RuCl_3$ is due to enhanced effective electron number, reduction of the carrier hopping barrier energy, and successful hindrance for generation of HDCs by the electron-doped Ru^{2+} site after intercalation.[58] However, clear elucidation of enhanced photoresponse in the doped Mott insulator $RuCl_3$ should be further studied.

CONCLUSION

In summary, we suggested an approach to engineer the bandgap using charge doping in a layered Mott insulator, α-$RuCl_3$. In contrast to conventional layered semiconductors, the excessive carrier doping in α-$RuCl_3$ did not lead to metallic transition, which instead leads to effective bandgap reduction.

As a layered Mott insulator, the optical absorption of α-$RuCl_3$ was altered *via* a facile and spontaneous intercalation method. With organic ion (TMA^+) intercalation, the intercalation superlattice showed exceptional stability in the ambient air (more than four months), unlike in the intercalation of an alkali metal ion. Due to localized electron transfer during intercalation, the optical absorption peak of α-$RuCl_3$ was changed from 1.2 eV to 0.7 eV. Surprisingly, the reduced optical bandgap was independent of the relative composition of $(TMA^+)_x$. The change in optical absorption was mainly attributed to the distinct DOS generated in the valence band with negligible shift of the conduction band.

To further prove optoelectronic properties enhancement *via* intercalation, the demonstration of photodetectors using pristine $RuCl_3$ and the $(TMA^+)_xRuCl_3$ superlattice as channel materials was conducted. As pristine $RuCl_3$ commenced to absorb light from 1 eV, the pristine photodetector had no photoresponse at 1600 nm laser (0.77 eV). At 1100 nm illumination (1.12 eV), it showed 4.2×10^{-6} A/W of photoresponsivity and 25 ms of response time. With a bandgap shift to 0.7 eV *via* intercalation, the photodetector using the $(TMA^+)_xRuCl_3$ superlattice showed a stable photoresponse in the NIR range. The photoresponsivity was calculated to be 1.0×10^{-4} A/W with 8 ms of typical response time, which showed 50 times higher responsivity and 3 times faster response time than those of pristine photodetectors. The relatively fast response time (<8 ms) of intercalated photodetectors suggested that the photocurrent mainly resulted from the band-to-band transition, not from the bolometric effects or trap states.

This stable and effective method of bandgap engineering using intercalation of layered Mott insulators could help to overcome disadvantage of optoelectronic properties in the Mott insulator. Moreover, charge doping to Mott insulators through intercalation suggested this study can be very useful without generation of crystalline defects in host materials for not only development of optoelectronic device but also realization of theoretically predicted high-temperature superconductivity, quantum spin liquids, and Majorana fermions,[59−61] which would further contribute to future quantum devices.

EXPERIMENTAL METHODS

Chemical Vapor Transport Growth of Single-Crystalline α-$RuCl_3$. First, $RuCl_3$ (Sigma-Aldrich, Ru contents 45−55%) was sealed with a quartz ampule under vacuum (pressure $\sim 10^{-3}$ Torr) and annealed at 500 °C for 48 h. Then we resealed about 1 g of the above annealed $RuCl_3$ as a starting precursor under vacuum in a silica ampule with an inner/outer diameter of 12.5/13.75 mm and a length of 120 mm. For the vapor transport growth, the ampule was put horizontally into a single-zone tube furnace, and we ramped up the temperature of the hot end, where $RuCl_3$ was located, in the ampule to 700 °C for 12 h, where it was kept for 7 days and cooled to room temperature for 12 h. α-$RuCl_3$ crystals were typically formed at the cold end of the ampule with a temperature of 670 °C.

Device Fabrication. Cr/Au (10/30 nm) patterned electrodes were deposited on a 300 nm SiO_2/Si substrate by an e-beam evaporator. The mechanically exfoliated α-$RuCl_3$ with an 80−100 nm height was positioned on the prepatterned electrodes.

Intercalation. The facile intercalation of α-$RuCl_3$ was done in ambient air conditions. The mechanically exfoliated flakes on different substrates or the *gold-contacted* α-$RuCl_3$ device were immersed in a saturated tetramethylammonium bromide solution in propylene carbonate. The solution was heated to 90−120 °C for 2−5 h depending on the substrate. Then, the exfoliated flakes or devices were rinsed with acetone and IPA, followed by N_2 blowing.

Characterization. Laboratory-based XRD equipment (Smartlab, Rigaku) was used for interlayer distance calculation and one-dimensional electron density analysis. The relationship between the structure factor and electron density is explained in the Supporting Information.

AFM equipment (Innova-Labram HR800) was used to measure the thickness of pristine $RuCl_3$ and intercalated $RuCl_3$. The cross-sectional samples were prepared by a focused ion beam (FIB, FEI Helios NanoLab 450) to observe interlayer spacing change after intercalation. Then, HR-TEM images were obtained using a FEI Titan^3 G2 60-300 operating at 200 kV.

The UV−vis absorption spectrum was measured in the wavelength range 300−3000 nm using an integrating sphere spectrometer (Lambda 1050) at KARA (KAIST Analysis Center for Research Advancement). A 2.5 cm × 2.5 cm quartz substrate was used as a reference, and mechanically exfoliated α-$RuCl_3$ on a quartz substrate was used as a pristine sample. For the intercalation sample, the pristine sample was immersed in a TMA^+Br^-/PC solution for a few hours and rinsed with acetone and IPA, followed by N_2 blowing.

The STM and spectroscopy (Unisoku Co., USM 1300) experiments were carried out using low-temperature STM in an ultra-high-vacuum chamber, whose base pressure was below 1×10^{-10} Torr. Pristine or intercalated $RuCl_3$ crystals were loaded into the STM chamber and quenched down to ~78 K for the STM and spectroscopy measurements. A Pt−Ir alloy probe tip was used to measure the STM.

PiFM measurements were carried out by the VistaScope from Molecular Vista Inc. (San Jose, CA, USA), which was coupled to a Laser Tune QCL system from Block Engineering with a tuning range from 750 to 1900 cm^{-1} and a wavenumber resolution of 1 cm^{-1}. The 40 ns pulsed beam was side-illuminated at a 40 degree angle from the sample surface by a parabolic mirror, which has a numerical aperture

https://doi.org/10.1021/acsnano.1c06752
ACS Nano 2021, 15, 18113−18124

(NA) of around 0.4. The average illumination power of the QCL source is approximately 2 mW with a 2λ diameter focal spot. The microscope was operated in noncontact/tapping mode with a PDMS-less gold-coated Si cantilever obtained from NCH-Au PiFM at Molecular Vista Inc. The 40 ns pulsed QCL beam was modulated at f_m = 1.82 MHz (= f_1 + f_2) by tuning its repetition rate to the sum frequency of the cantilever's first and second eigenmodes, f_1 and f_2. The free oscillating noncontact/tapping amplitude was typically around 2 nm at the second eigenmode of the cantilever (typically around 1.57 MHz), and the PiFM amplitude was demodulated at the fundamental resonance (typically around 250 kHz).

Pristine and intercalated $RuCl_3$ crystals were opened in a glovebox filled with Ar gas and transferred into an XPS/UPS adaptable sample-transfer-vessel to prevent surface reaction with air. The Ar-filled vessel was connected to the system and pumped down before loading samples into the system. XPS and UPS measurements were performed using a PHI5000 Versa Probe II (Ulvac-PHI). The base pressure was below 3×10^{-10} Torr. A monochromatic Al Kα source (1486.6 eV) and windowless He discharge light source with He(I) emission at 21.2 eV were used as light sources for XPS and UPS, respectively. The binding energy scale for XPS was calibrated using sputtered Au, Ag, and Cu films based on ISO 15472. The spectrometer work function for UPS was monitored by measuring the Fermi level with a sputtered Au sample.

To estimate transport characteristics, the devices were biased by a Keithley 4200 semiconductor parameter analyzer system. The low-temperature measurements were performed in a cryostation s50 (Montana Instruments). For photoresponse-characteristic investigations, a supercontinuum laser source (Fianium) and SP2150 monochromator (Teledyne Prinston Instruments) were used as a light source. An SH05 shutter (Thorlabs) was used for systematic control of light.

Computational Details. We performed first-principles DFT calculations within the generalized gradient approximations of Perdew, Burke, and Ernzerhof (PBE).[62] We used a plane-wave basis and projector augmented-wave (PAW)[63,64] pseudopotentials with the Vienna *ab initio* Simulation Package (VASP) code.[65−68] To include the effect of the van der Waals dispersive interactions on structural properties, we performed structural relaxations with Grimme's D3 method[69] as implemented in VASP. SOC effects were included self-consistently during all electronic and structural relaxations. The initial crystal (monoclinic $C2/m$) and magnetic (zigzag antiferromagnetic) structures of α-$RuCl_3$ we consider here were obtained from a previous experimental study.[45] For intercalated $RuCl_3$, we removed one $RuCl_3$ layer and added two TMA molecules in the 1 × 1 × 2 supercell. The effective Hubbard U_{eff}(U−J) of 2.0 eV was chosen on the basis of the previous DFT study.[70] For all calculations, we used (i) a 5 × 3 × 5 k-point grid for pristine $RuCl_3$ and a 5 × 3 × 3 k-point grid for intercalated $RuCl_3$ and (ii) a 500 eV plane-wave cutoff energy. We explicitly treated 14 valence electrons for Ru ($4p^6 4d^7 5s^1$), seven for Cl ($3s^2 3p^5$), five for N ($2s^2 2p^3$), four for C ($2s^2 2p^2$), and one for H($1s^1$). All structural relaxations are performed with a Gaussian smearing of 0.05 eV.[71] The ions are relaxed until the Hellmann−Feynman forces were less than 0.01 eV Å^{-1}. We also optimized the unit cell volumes.

ASSOCIATED CONTENT

Supporting Information

The Supporting Information is available free of charge at https://pubs.acs.org/doi/10.1021/acsnano.1c06752.

Band structure of α-$RuCl_3$, VSM analysis of pristine and intercalated α-$RuCl_3$, intercalation method schematic, AFM analysis, FT-IR spectrum of TMAB and PiFM experimental setup, intercalation time-dependent optical absorption and structural change, XPS analysis, electrical transport of pristine and intercalated α-$RuCl_3$ device and their optical images, quantification analysis based on XPS analysis, and information about 1D electron density mapping (PDF)

AUTHOR INFORMATION

Corresponding Authors

Kibum Kang − *Department of Materials Science and Engineering, Korea Advanced Institute of Science and Technology (KAIST), Daejeon 34141, Korea;* orcid.org/0000-0003-1674-1826; Email: kibumkang@kaist.ac.kr

Seungwoo Song − *Operando Methodology and Measurement Team, Interdisciplinary Materials Measurement Institute, Korea Research Institute of Standards and Science (KRISS), Daejeon 34113, Korea;* orcid.org/0000-0002-8524-3444; Email: swsong@kriss.re.kr

Authors

Min-kyung Jo − *Operando Methodology and Measurement Team, Interdisciplinary Materials Measurement Institute, Korea Research Institute of Standards and Science (KRISS), Daejeon 34113, Korea; Department of Materials Science and Engineering, Korea Advanced Institute of Science and Technology (KAIST), Daejeon 34141, Korea*

Hoseok Heo − *Inorganic Material Lab., Samsung Advanced Institute of Technology (SAIT), Suwon 16678, Korea*

Jung-Hoon Lee − *Computational Science Research Center, Korea Institute of Science and Technology (KIST), Seoul 02792, Korea*

Seungwook Choi − *Operando Methodology and Measurement Team, Interdisciplinary Materials Measurement Institute, Korea Research Institute of Standards and Science (KRISS), Daejeon 34113, Korea*

Ansoon Kim − *Operando Methodology and Measurement Team, Interdisciplinary Materials Measurement Institute, Korea Research Institute of Standards and Science (KRISS), Daejeon 34113, Korea;* orcid.org/0000-0002-2702-7073

Han Beom Jeong − *Department of Materials Science and Engineering, Korea Advanced Institute of Science and Technology (KAIST), Daejeon 34141, Korea*

Hu Young Jeong − *UNIST Central Research Facilities (UCRF) and Department of Materials Science and Engineering, Ulsan National Institute of Science and Technology (UNIST), Ulsan 44919, Korea;* orcid.org/0000-0002-5550-5298

Jong Min Yuk − *Department of Materials Science and Engineering, Korea Advanced Institute of Science and Technology (KAIST), Daejeon 34141, Korea;* orcid.org/0000-0002-4677-7363

Daejin Eom − *Atom-scale Measurement Team, Advanced Instrumentation Institute, Korea Research Institute of Standards and Science (KRISS), Daejeon 34113, Korea;* orcid.org/0000-0001-6011-1149

Junghoon Jahng − *Hyperspectral Nano-imaging Lab, Interdisciplinary Materials Measurement Institute, Korea Research Institute of Standards and Science (KRISS), Daejeon 34113, Korea;* orcid.org/0000-0002-5745-9686

Eun Seong Lee − *Hyperspectral Nano-imaging Lab, Interdisciplinary Materials Measurement Institute, Korea Research Institute of Standards and Science (KRISS), Daejeon 34113, Korea;* orcid.org/0000-0001-9444-1824

In-young Jung − *Operando Methodology and Measurement Team, Interdisciplinary Materials Measurement Institute, Korea Research Institute of Standards and Science (KRISS), Daejeon 34113, Korea*

Seong Rae Cho − *Department of Materials Science and Engineering, Korea Advanced Institute of Science and Technology (KAIST), Daejeon 34141, Korea*

https://doi.org/10.1021/acsnano.1c06752
ACS Nano 2021, 15, 18113−18124

Jeongtae Kim − *Operando Methodology and Measurement Team, Interdisciplinary Materials Measurement Institute, Korea Research Institute of Standards and Science (KRISS), Daejeon 34113, Korea*

Seorin Cho − *Department of Materials Science and Engineering, Korea Advanced Institute of Science and Technology (KAIST), Daejeon 34141, Korea*

Complete contact information is available at: https://pubs.acs.org/10.1021/acsnano.1c06752

Author Contributions

The manuscript was written through contributions of all authors. All authors have given approval to the final version of the manuscript.

Funding

This research was supported by Establishment of the Foundation for Advanced Materials Measurement Platform funded by Korea Research Institute of Standards and Science (KRISS-2021-GP2021-0011) and the National R&D Program through the National Research Foundation of Korea (NRF) funded by the Ministry of Science and ICT (Grant Nos. 2020R1C1C1014257, 2021R1C1C1007292), and Korea Institute of Science and Technology (KIST) Institutional Program (2 V07080-19-P148). Computations and resources were supported by the KIST Institutional Program (Project No. 2E30460) and KISTI Supercomputing Centre (Project No. KSC-2020-CRE-0361).

Notes

The authors declare no competing financial interest.

ACKNOWLEDGMENTS

We thank Prof. H. Park for single-crystal synthesis using his lab's facility and discussions.

REFERENCES

(1) Song, C.; Noh, G.; Kim, T. S.; Kang, M.; Song, H.; Ham, A.; Jo, M. K.; Cho, S.; Chai, H. J.; Cho, S. R.; Cho, K.; Park, J.; Song, S.; Song, I.; Bang, S.; Kwak, J. Y.; Kang, K. Growth and Interlayer Engineering of 2D Layered Semiconductors for Future Electronics. *ACS Nano* **2020**, *14* (12), 16266−16300.

(2) Yao, J.; Koski, K. J.; Luo, W.; Cha, J. J.; Hu, L.; Kong, D.; Narasimhan, V. K.; Huo, K.; Cui, Y. Optical Transmission Enhacement through Chemically Tuned Two-Dimensional Bismuth Chalcogenide Nanoplates. *Nat. Commun.* **2014**, *5*, 1−7.

(3) Wang, N.; Tang, H.; Shi, M.; Zhang, H.; Zhuo, W.; Liu, D.; Meng, F.; Ma, L.; Ying, J.; Zou, L.; Sun, Z.; Chen, X. Transition from Ferromagnetic Semiconductor to Ferromagnetic Metal with Enhanced Curie Temperature in $Cr_2Ge_2Te_6$ *via* Organic Ion Intercalation. *J. Am. Chem. Soc.* **2019**, *141* (43), 17166−17173.

(4) Weller, T. E.; Ellerb, M.; Saxena, S. S.; Smith, R. P.; Skipper, N. T. Superconductivity in the Intercalated Graphite Compounds C_6Yb and C_6Ca. *Nat. Phys.* **2005**, *1* (1), 39−41.

(5) Ma, L. K.; Shi, M. Z.; Kang, B. L.; Peng, K. L.; Meng, F. B.; Zhu, C. S.; Cui, J. H.; Sun, Z. L.; Ma, D. H.; Wang, H. H.; Lei, B.; Wu, T.; Chen, X. H. Quasi-Two-Dimensional Superconductivity in $SnSe_2$ *via* Organic Ion Intercalation. *Phys. Rev. Mater.* **2020**, *4* (12), 1−7.

(6) Wan, C.; Gu, X.; Dang, F.; Itoh, T.; Wang, Y.; Sasaki, H.; Kondo, M.; Koga, K.; Yabuki, K.; Snyder, G. J.; Yang, R.; Koumoto, K. Flexible *n*-Type Thermoelectric Materials by Organic Intercalation of Layered Transition Metal Dichalcogenide TiS_2. *Nat. Mater.* **2015**, *14* (6), 622−627.

(7) Wang, C.; He, Q.; Halim, U.; Liu, Y.; Zhu, E.; Lin, Z.; Xiao, H.; Duan, X.; Feng, Z.; Cheng, R.; Weiss, N. O.; Ye, G.; Huang, Y. C.; Wu, H.; Cheng, H. C.; Shakir, I.; Liao, L.; Chen, X.; Goddard, W. A.; Huang, Y.; et al. Monolayer Atomic Crystal Molecular Superlattices. *Nature* **2018**, *555* (7695), 231−236.

(8) He, Q.; Lin, Z.; Ding, M.; Yin, A.; Halim, U.; Wang, C.; Liu, Y.; Cheng, H. C.; Huang, Y.; Duan, X. *In Situ* Probing Molecular Intercalation in Two-Dimensional Layered Semiconductors. *Nano Lett.* **2019**, *19* (10), 6819−6826.

(9) Zhou, J.; Lin, Z.; Ren, H.; Duan, X.; Shakir, I.; Huang, Y.; Duan, X. Layered Intercalation Materials. *Adv. Mater.* **2021**, *33* (25), 1−23.

(10) Lin, J.; Chen, H.; Ma, D.; Gong, Y.; Li, Z.; Li, D.; Song, Y.; Zhang, F.; Li, J.; Wang, H.; Wang, Y.; Zhang, H. Band Structure Tuning of α-MoO_3 by Tin Intercalation for Ultrafast Photonic Applications. *Nanoscale* **2020**, *12* (45), 23140−23149.

(11) Shen, P. C.; Su, C.; Lin, Y.; Chou, A. S.; Cheng, C. C.; Park, J. H.; Chiu, M. H.; Lu, A. Y.; Tang, H. L.; Tavakoli, M. M.; Pitner, G.; Ji, X.; Cai, Z.; Mao, N.; Wang, J.; Tung, V.; Li, J.; Bokor, J.; Zettl, A.; Wu, C. I.; et al. Ultralow Contact Resistance between Semimetal and Monolayer Semiconductors. *Nature* **2021**, *593* (7858), 211−217.

(12) Li, T.; Guo, W.; Ma, L.; Li, W.; Yu, Z.; Han, Z.; Gao, S.; Liu, L.; Fan, D.; Wang, Z.; Yang, Y.; Lin, W.; Luo, Z.; Chen, X.; Dai, N.; Tu, X.; Pan, D.; Yao, Y.; Wang, P.; Nie, Y.; et al. Epitaxial Growth of Wafer-Scale Molybdenum Disulfide Semiconductor Single Crystals on Sapphire. *Nat. Nanotechnol.* **2021**, DOI: 10.1038/s41565-021-00963-8.

(13) Cao, G.; Meng, P.; Chen, J.; Liu, H.; Bian, R.; Zhu, C.; Liu, F.; Liu, Z. 2D Material Based Synaptic Devices for Neuromorphic Computing. *Adv. Funct. Mater.* **2021**, *31* (4), 1−29.

(14) Zhou, F.; Zhou, Z.; Chen, J.; Choy, T. H.; Wang, J.; Zhang, N.; Lin, Z.; Yu, S.; Kang, J.; Wong, H. S. P.; Chai, Y. Optoelectronic Resistive Random Access Memory for Neuromorphic Vision Sensors. *Nat. Nanotechnol.* **2019**, *14* (8), 776−782.

(15) McGlynn, J. C.; Dankwort, T.; Kienle, L.; Bandeira, N. A. G.; Fraser, J. P.; Gibson, E. K.; Cascallana-Matías, I.; Kamarás, K.; Symes, M. D.; Miras, H. N.; Ganin, A. Y. The Rapid Electrochemical Activation of $MoTe_2$ for the Hydrogen Evolution Reaction. *Nat. Commun.* **2019**, *10* (1), 4916.

(16) Li, H.; Tsai, C.; Koh, A. L.; Cai, L.; Contryman, A. W.; Fragapane, A. H.; Zhao, J.; Han, H. S.; Manoharan, H. C.; Abild-Pedersen, F.; Nørskov, J. K.; Zheng, X. Activating and Optimizing MoS_2 Basal Planes for Hydrogen Evolution through the Formation of Strained Sulphur Vacancies. *Nat. Mater.* **2016**, *15* (3), 364.

(17) Tan, T.; Jiang, X.; Wang, C.; Yao, B.; Zhang, H. 2D Material Optoelectronics for Information Functional Device Applications: Status and Challenges. *Adv. Sci.* **2020**, *7* (11), 2000058.

(18) Chaves, A.; Azadani, J. G.; Alsalman, H.; da Costa, D. R.; Frisenda, R.; Chaves, A. J.; Song, S. H.; Kim, Y. D.; He, D.; Zhou, J.; Castellanos-Gomez, A.; Peeters, F. M.; Liu, Z.; Hinkle, C. L.; Oh, S. H.; Ye, P. D.; Koester, S. J.; Lee, Y. H.; Avouris, P.; Wang, X.; et al. Bandgap Engineering of Two-Dimensional Semiconductor Materials. *npj 2D Mater. Appl.* **2020**, *4* (1), 29.

(19) Kappera, R.; Voiry, D.; Yalcin, S. E.; Branch, B.; Gupta, G.; Mohite, A. D.; Chhowalla, M. Phase-Engineered Low-Resistance Contacts for Ultrathin MoS_2 Transistors. *Nat. Mater.* **2014**, *13* (12), 1128−1134.

(20) Kasirga, T. S.; Sun, D.; Park, J. H.; Coy, J. M.; Fei, Z.; Xu, X.; Cobden, D. H. Photoresponse of a Strongly Correlated Material Determined by Scanning Photocurrent Microscopy. *Nat. Nanotechnol.* **2012**, *7* (11), 723−727.

(21) Koitzsch, A.; Habenicht, C.; Müller, E.; Knupfer, M.; Büchner, B.; Kandpal, H. C.; Van Den Brink, J.; Nowak, D.; Isaeva, A.; Doert, T. Jeff Description of the Honeycomb Mott Insulator α-$RuCl_3$. *Phys. Rev. Lett.* **2016**, *117* (12), 1−5.

(22) Binotto, L.; Pollini, I.; Spinolo, G. Optical and Transport Properties of the Magnetic Semiconductor α-$RuCl_3$. *Phys. Status Solidi B* **1971**, *44* (1), 245−252.

(23) Zhou, X.; Li, H.; Waugh, J. A.; Parham, S.; Kim, H. S.; Sears, J. A.; Gomes, A.; Kee, H. Y.; Kim, Y. J.; Dessau, D. S. Angle-Resolved Photoemission Study of the Kitaev Candidate α-$RuCl_3$. *Phys. Rev. B: Condens. Matter Mater. Phys.* **2016**, *94* (16), 1−5.

(24) Koitzsch, A.; Habenicht, C.; Müller, E.; Knupfer, M.; Büchner, B.; Kretschmer, S.; Richter, M.; Van Den Brink, J.; Börrnert, F.; Nowak, D.; Isaeva, A.; Doert, T. Nearest-Neighbor Kitaev Exchange Blocked by Charge Order in Electron-Doped α-$RuCl_3$. *Phys. Rev. Mater.* **2017**, *1* (5), 1−6.
(25) Imai, Y.; Konno, K.; Hasegawa, Y.; Aoyama, T.; Ohgushi, K. Hydrated Lithium Intercalation into the Kitaev Spin Liquid Candidate Material α-$RuCl_3$. *Phys. Rev. B: Condens. Matter Mater. Phys.* **2019**, *99* (24), 1−7.
(26) Orenstein, J.; Millis, A. J. Advances in the Physics of High-Temperature Superconductivity. *Science* **2000**, *288* (5465), 468−474.
(27) Shin, Y. S.; Lee, K.; Duong, D. L.; Kim, J. S.; Kang, W. T.; Kim, J. E.; Won, U. Y.; Lee, I.; Lee, H.; Heo, J.; Lee, Y. H.; Yu, W. J. Li Intercalation Effects on Interface Resistances of High-Speed and Low-Power WSe_2 Field-Effect Transistors. *Adv. Funct. Mater.* **2020**, *30* (45), 1−9.
(28) Lenarčič, Z.; Prelovšek, P. Ultrafast Charge Recombination in a Photoexcited Mott-Hubbard Insulator. *Phys. Rev. Lett.* **2013**, *111* (1), 1−5.
(29) Okamoto, H.; Miyagoe, T.; Kobayashi, K.; Uemura, H.; Nishioka, H.; Matsuzaki, H.; Sawa, A.; Tokura, Y. Ultrafast Charge Dynamics in Photoexcited Nd_2CuO_4 and La_2CuO_4 Cuprate Compounds Investigated by Femtosecond Absorption Spectroscopy. *Phys. Rev. B: Condens. Matter Mater. Phys.* **2010**, *82* (6), 1−4.
(30) Kim, B. J.; Jin, H.; Moon, S. J.; Kim, J. Y.; Park, B. G.; Leem, C. S.; Yu, J.; Noh, T. W.; Kim, C.; Oh, S. J.; Park, J. H.; Durairaj, V.; Cao, G.; Rotenberg, E. Novel J_{eff}=1/2 Mott State Induced by Relativistic Spin-Orbit Coupling in Sr_2IrO_4. *Phys. Rev. Lett.* **2008**, *101* (7), 1−4.
(31) Shitade, A.; Katsura, H.; Kuneš, J.; Qi, X. L.; Zhang, S. C.; Nagaosa, N. Quantum Spin Hall Effect in a Transition Metal Oxide Na_2IrO_3. *Phys. Rev. Lett.* **2009**, *102* (25), 3−6.
(32) Lu, C.; Liu, J. M. The J_{eff} = 1/2 Antiferromagnet Sr_2IrO_4: A Golden Avenue toward New Physics and Functions. *Adv. Mater.* **2019**, *32* (27), 1−15.
(33) Kim, J.; Said, A. H.; Casa, D.; Upton, M. H.; Gog, T.; Daghofer, M.; Jackeli, G.; Van Den Brink, J.; Khaliullin, G.; Kim, B. J. Large Spin-Wave Energy Gap in the Bilayer Iridate $Sr_3Ir_2O_7$: Evidence for Enhanced Dipolar Interactions near the Mott Metal-Insulator Transition. *Phys. Rev. Lett.* **2012**, *109* (15), 1−5.
(34) Gretarsson, H.; Clancy, J. P.; Liu, X.; Hill, J. P.; Bozin, E.; Singh, Y.; Manni, S.; Gegenwart, P.; Kim, J.; Said, A. H.; Casa, D.; Gog, T.; Upton, M. H.; Kim, H. S.; Yu, J.; Katukuri, V. M.; Hozoi, L.; Van Den Brink, J.; Kim, Y. J. Crystal-Field Splitting and Correlation Effect on the Electronic Structure of A_2IrO_3. *Phys. Rev. Lett.* **2013**, *110* (7), 1−5.
(35) Plumb, K. W.; Clancy, J. P.; Sandilands, L. J.; Shankar, V. V.; Hu, Y. F.; Burch, K. S.; Kee, H. Y.; Kim, Y. J. α-$RuCl_3$: A Spin-Orbit Assisted Mott Insulator on a Honeycomb Lattice. *Phys. Rev. B: Condens. Matter Mater. Phys.* **2014**, *90* (4), 1−5.
(36) Banerjee, A.; Bridges, C. A.; Yan, J. Q.; Aczel, A. A.; Li, L.; Stone, M. B.; Granroth, G. E.; Lumsden, M. D.; Yiu, Y.; Knolle, J.; Bhattacharjee, S.; Kovrizhin, D. L.; Moessner, R.; Tennant, D. A.; Mandrus, D. G.; Nagler, S. E. Proximate Kitaev Quantum Spin Liquid Behaviour in a Honeycomb Magnet. *Nat. Mater.* **2016**, *15* (7), 733−740.
(37) Sandilands, L. J.; Tian, Y.; Reijnders, A. A.; Kim, H. S.; Plumb, K. W.; Kim, Y. J.; Kee, H. Y.; Burch, K. S. Spin-Orbit Excitations and Electronic Structure of the Putative Kitaev Magnet α-$RuCl_3$. *Phys. Rev. B: Condens. Matter Mater. Phys.* **2016**, *93* (7), 1−7.
(38) Sinn, S.; Kim, C. H.; Kim, B. H.; Lee, K. D.; Won, C. J.; Oh, J. S.; Han, M.; Chang, Y. J.; Hur, N.; Sato, H.; Park, B. G.; Kim, C.; Do Kim, H.; Noh, T. W. Electronic Structure of the Kitaev Material α-$RuCl_3$ Probed by Photoemission and Inverse Photoemission Spectroscopies. *Sci. Rep.* **2016**, *6*, 1−7.
(39) Kim, H. S.; Shankar, V.; Catuneanu, A.; Kee, H. Y. Kitaev Magnetism in Honeycomb $RuCl_3$ with Intermediate Spin-Orbit Coupling. *Phys. Rev. B: Condens. Matter Mater. Phys.* **2015**, *91* (24), DOI: 10.1103/PhysRevB.91.241110.
(40) Hashimoto, M.; Vishik, I. M.; He, R. H.; Devereaux, T. P.; Shen, Z. X. Energy Gaps in High-Transitionerature Cuprate Superconductors. *Nat. Phys.* **2014**, *10* (7), 483−495.
(41) Katase, T.; Hiramatsu, H.; Kamiya, T.; Hosono, H. Electric Double-Layer Transistor Using Layered Iron Selenide Mott Insulator $TlFe_{1.6}Se_2$. *Proc. Natl. Acad. Sci. U. S. A.* **2014**, *111* (11), 3979−3983.
(42) Cai, P.; Ruan, W.; Peng, Y.; Ye, C.; Li, X.; Hao, Z.; Zhou, X.; Lee, D. H.; Wang, Y. Visualizing the Evolution from the Mott Insulator to a Charge-Ordered Insulator in Lightly Doped Cuprates. *Nat. Phys.* **2016**, *12* (11), 1047−1051.
(43) Battisti, I.; Bastiaans, K. M.; Fedoseev, V.; De La Torre, A.; Iliopoulos, N.; Tamai, A.; Hunter, E. C.; Perry, R. S.; Zaanen, J.; Baumberger, F.; Allan, M. P. Universality of Pseudogap and Emergent Order in Lightly Doped Mott Insulators. *Nat. Phys.* **2017**, *13* (1), 21−25.
(44) Keimer, B.; Kivelson, S. A.; Norman, M. R.; Uchida, S.; Zaanen, J. From Quantum Matter to High-Temperature Superconductivity in Copper Oxides. *Nature* **2015**, *518* (7538), 179−186.
(45) Johnson, R. D.; Williams, S. C.; Haghighirad, A. A.; Singleton, J.; Zapf, V.; Manuel, P.; Mazin, I. I.; Li, Y.; Jeschke, H. O.; Valentí, R.; Coldea, R. Monoclinic Crystal Structure of α-$RuCl_3$ and the Zigzag Antiferromagnetic Ground State. *Phys. Rev. B: Condens. Matter Mater. Phys.* **2015**, *92* (23), 1−12.
(46) Sun, J.; Wang, Y.; Guo, S.; Wan, B.; Dong, L.; Gu, Y.; Song, C.; Pan, C.; Zhang, Q.; Gu, L.; Pan, F.; Zhang, J. Lateral 2D WSe_2 *p*−*n* Homojunction Formed by Efficient Charge-Carrier-Type Modulation for High-Performance Optoelectronics. *Adv. Mater.* **2020**, *32* (9), 1−9.
(47) Wang, L.; Rocci-Lane, M.; Brazis, P.; Kannewurf, C. R.; Kim, Y. Il; Lee, W.; Choy, J. H.; Kanatzidis, M. G. α-$RuCl_3$/Polymer Nanocomposites: The First Group of Intercalative Nanocoraposites with Transition Metal Halides. *J. Am. Chem. Soc.* **2000**, *122* (28), 6629−6640.
(48) Nowak, D.; Morrison, W.; Wickramasinghe, H. K.; Jahng, J.; Potma, E.; Wan, L.; Ruiz, R.; Albrecht, T. R.; Schmidt, K.; Frommer, J.; Sanders, D. P.; Park, S. Nanoscale Chemical Imaging by Photoinduced Force Microscopy. *Sci. Adv.* **2016**, *2* (3), DOI: 10.1126/sciadv.1501571.
(49) Sylvestre, J. P.; Poulin, S.; Kabashin, A. V.; Sacher, E.; Meunier, M.; Luong, J. H. T. Surface Chemistry of Gold Nanoparticles Produced by Laser Ablation in Aqueous Media. *J. Phys. Chem. B* **2004**, *108* (43), 16864−16869.
(50) McEvoy, A. J. ESCA Spectrum and Band Structure of Ruthenium Chloride. *Phys. Status Solidi* **1982**, *71* (2), 569−574.
(51) Guizzetti, G.; Reguzzoni, E.; Pollini, I. Fundamental Optical Properties of α-$RuCl_3$. *Phys. Lett. A* **1979**, *70* (1), 34−36.
(52) Weber, D.; Schoop, L. M.; Duppel, V.; Lippmann, J. M.; Nuss, J.; Lotsch, B. V. Magnetic Properties of Restacked 2D Spin 1/2 Honeycomb $RuCl_3$ Nanosheets. *Nano Lett.* **2016**, *16* (6), 3578−3584.
(53) Zeng, L.; Tao, L.; Tang, C.; Zhou, B.; Long, H.; Chai, Y.; Lau, S. P.; Tsang, Y. H. High-Responsivity UV-Vis Photodetector Based on Transferable WS_2 Film Deposited by Magnetron Sputtering. *Sci. Rep.* **2016**, *6*, 1−8.
(54) Terashige, T.; Ono, T.; Miyamoto, T.; Morimoto, T.; Yamakawa, H.; Kida, N.; Ito, T.; Sasagawa, T.; Tohyama, T.; Okamoto, H. Doublon-Holon Pairing Mechanism *via* Exchange Interaction in Two-Dimensional Cuprate Mott Insulators. *Sci. Adv.* **2019**, *5* (6), 1−9.
(55) Matsuda, K.; Hirabayashi, I.; Kawamoto, K.; Nabatame, T.; Tokizaki, T.; Nakamura, A. Femtosecond Spectroscopic Studies of the Ultrafast Relaxation Process in the Charge-Transfer State of Insulating Cuprates. *Phys. Rev. B: Condens. Matter Mater. Phys.* **1994**, *50* (6), 4097−4101.
(56) Okamoto, H.; Miyagoe, T.; Kobayashi, K.; Uemura, H.; Nishioka, H.; Matsuzaki, H.; Sawa, A.; Tokura, Y. Photoinduced Transition from Mott Insulator to Metal in the Undoped Cuprates Nd_2CuO_4 and La_2CuO_4. *Phys. Rev. B: Condens. Matter Mater. Phys.* **2011**, *83* (12), 1−10.

(57) Gomi, H.; Takahashi, A.; Ueda, T.; Itoh, H.; Aihara, M. Photogenerated Holon-Doublon Cluster States in Strongly Correlated Low-Dimensional Electron Systems. *Phys. Rev. B: Condens. Matter Mater. Phys.* **2005**, *71* (4), 1−10.
(58) Uchida, S.; Ido, T.; Takagi, H.; Arima, T.; Tokura, Y.; Tajima, S. Optical Spectra of $La_{2-X}Sr_xCuO_4$: Effect of Carrier Doping on the Electronic Structure of the CuO_2 Plane. *Phys. Rev. B: Condens. Matter Mater. Phys.* **1991**, *43* (10), 7942−7954.
(59) Kelly, Z. A.; Gallagher, M. J.; McQueen, T. M. Electron Doping a Kagome Spin Liquid. *Phys. Rev. X* **2016**, *6* (4), 1−7.
(60) Chamorro, J. R.; McQueen, T. M.; Tran, T. T. Chemistry of Quantum Spin Liquids. *Chem. Rev.* **2021**, *121* (5), 2898−2934.
(61) Aasen, D.; Hell, M.; Mishmash, R. V.; Higginbotham, A.; Danon, J.; Leijnse, M.; Jespersen, T. S.; Folk, J. A.; Marcus, C. M.; Flensberg, K.; Alicea, J. Milestones toward Majorana-Based Quantum Computing. *Phys. Rev. X* **2016**, *6* (3), 1−28.
(62) Perdew, J. P.; Burke, K.; Ernzerhof, M. Generalized Gradient Approximation Made Simple. *Phys. Rev. Lett.* **1996**, *77* (18), 3865−3868.
(63) Blöchl, P. E. Projector Augmented-Wave Method. *Phys. Rev. B: Condens. Matter Mater. Phys.* **1994**, *50* (24), 17953−17979.
(64) Joubert, D. From Ultrasoft Pseudopotentials to the Projector Augmented-Wave Method. *Phys. Rev. B: Condens. Matter Mater. Phys.* **1999**, *59* (3), 1758−1775.
(65) Kresse, G.; Hafner, J. *Ab Initio* Molecular Dynamics for Liquid Metals. *Phys. Rev. B: Condens. Matter Mater. Phys.* **1993**, *47* (1), 558−561.
(66) Vargas-Hernández, R. A. Bayesian Optimization for Calibrating and Selecting Hybrid-Density Functional Models. *J. Phys. Chem. A* **2020**, *124* (20), 4053−4061.
(67) Kresse, G.; Furthmüller, J. Efficiency of *ab Initio* Total Energy Calculations for Metals and Semiconductors Using a Plane-Wave Basis Set. *Comput. Mater. Sci.* **1996**, *6* (1), 15−50.
(68) Kresse, G.; Hafner, J. *Ab Initio* Molecular-Dynamics Simulation of the Liquid-Metalamorphous- Semiconductor Transition in Germanium. *Phys. Rev. B: Condens. Matter Mater. Phys.* **1994**, *49* (20), 14251−14269.
(69) Allouche, A. Software News and Updates Gabedit — A Graphical User Interface for Computational Chemistry Softwares. *J. Comput. Chem.* **2011**, *32*, 174−182.
(70) Kim, H. S.; Kee, H. Y. Crystal Structure and Magnetism in α-$RuCl_3$: An *ab Initio* Study. *Phys. Rev. B: Condens. Matter Mater. Phys.* **2016**, *93* (15), 1−10.
(71) Elsässer, C.; Fähnle, M.; Chan, C. T.; Ho, K. M. Density-Functional Energies and Forces with Gaussian-Broadened Fractional Occupations. *Phys. Rev. B: Condens. Matter Mater. Phys.* **1994**, *49* (19), 13975−13978.

https://doi.org/10.1021/acsnano.1c06752
ACS Nano 2021, 15, 18113−18124